Ocean Engineering 238 (2021) 109682

Contents lists available at ScienceDirect

Ocean Engineering

journal homepage: www.elsevier.com/locate/oceaneng

Free surface and near-wall effects on the cloud cavitating flow over an axisymmetric projectile

Chang Xu [a,*], Jian Huang [b,c], Chao Yu [b,c], Yiwei Wang [b,c,**], Chenguang Huang [b,c], Boo Cheong Khoo [a]

[a] Department of Mechanical Engineering, National University of Singapore, 119260, Singapore
[b] Key Laboratory for Mechanics in Fluid Solid Coupling Systems, Institute of Mechanics, Chinese Academy of Sciences, 100190, Beijing, China
[c] School of Engineering Science, University of Chinese Academy of Sciences, 100049, Beijing, China

ARTICLE INFO

Keywords:
Unsteady cloud cavitation
Moderate cavitation number
Free surface effect
Near-wall effect

ABSTRACT

For high-speed underwater vehicles, cavitation can be one of the most important speed barriers. The cavitating flow can be even complex when an underwater vehicle is sailing close to the free surface/wall. In this study, the mutual effects of the free surface and near-wall on the cloud cavitating flow that surrounds an axisymmetric projectile are investigated by water tank experiment and the computational fluids dynamics (CFD). The Split-Hopkinson pressure bar (SHPB) technology is applied in the experiment to accelerate the projectile in a short time. In our numerical approach, the volume of fluid (VOF) method, the large eddy simulation (LES) turbulence model, and the Zwart-Gerber-Belamri (ZGB) cavitation model are used. The cloud cavitating flow under the free surface/wall effect is investigated by changing the distance between the projectile and free surface (d_f) or wall (d_w). Both the experiment and the simulation show that the unstable cavity evolution includes four stages induced by the re-entrant jet: cavity growth, re-entrant jet, cavity shedding and collapsing. The results further show that as d_f decreases, the cavity length is shorter and the cavity becomes more stable; as d_w decreases, the cavity length is longer and the cavity becomes less stable. By understanding the free surface/wall effect on the stability of the cloud cavitating flow, the parameters space spanned by d_f and d_w can be divided into several distinct flow regimes, in which the entire shedding cavity (symmetry/asymmetry), steady and non-shedding cavity, partial cavity shedding, and ventilated cavity are identified.

1. Introduction

For typical high-speed underwater vehicles, the unstable cavitating flow over the vehicles and its interaction with free surfaces and nearby walls can affect the cruise. Through the development of shape, the cavitation phenomena can be classified into incipient cavitation, sheet cavitation, cloud cavitation, and supercavitation with a change of cavitation number from high to low (Franc and Michel, 2004; Wang et al., 2001). For cloud cavitating flow that occurs at moderate cavitation number, the cavitation instability (such as cavity shedding and collapsing) may damage the structure or affect navigation. Various experimental and numerical methods have been used to analyze cavitation in past studies. However, most of the relevant studies focus on the characteristics and mechanisms of the unsteady cloud cavitating flow around the model in deep water (Yuet al., 2014; Owis and Nayfeh, 2004), the study on the cavitating flow near the free surface/wall is limited in the literature, and the understanding of the effects is still inadequate. To study the influence of cavitating flow on the performance of navigation vehicles, we should consider the significant boundaries such as free surface and bottom wall near the cavitating flow. The mechanism involved should be investigated to determine how to control the mutual effects in engineering applications.

Cavitation has always been at the forefront of research (Robert et al., 1970; Brennen, 2013). Experiments on cavitating flow are usually performed using water tunnel (Leroux et al., 2005) or water tank tests (Yan-Peng et al., 2011). Nevertheless, flow motion and cavity structure can be observed through experiments. Measurement technologies are used to measure the detailed parameters in the cavity, such as pressure,

* Corresponding author.
** Corresponding author. Key Laboratory for Mechanics in Fluid Solid Coupling Systems, Institute of Mechanics, Chinese Academy of Sciences, 100190, Beijing, China.
E-mail addresses: e0348786@u.nus.edu (C. Xu), wangyw@imech.ac.cn (Y. Wang).

https://doi.org/10.1016/j.oceaneng.2021.109682
Received 6 May 2021; Received in revised form 23 July 2021; Accepted 11 August 2021
Available online 20 August 2021

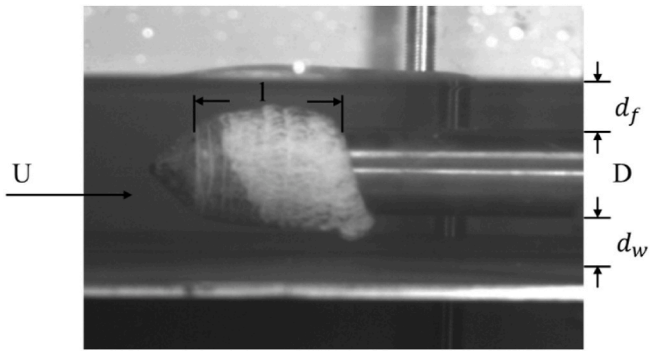

Fig. 1. Typical cloud cavitating flow over the projectile. D is the projectile diameter, U is the free stream velocity, d_f is the distance between the upper surface of the projectile and free surface, d_w is the distance between the lower surface of the projectile and bottom wall, and l is the cavity length.

density, and speed. For example, high-speed camera, particle image velocimetry (PIV) (Dular et al., 2004, 2005), and X-ray imaging (Heindel, 2011) are widely used in the measurement process. Experimental results indicate that numerical methods could help researchers discover the cavitating flow structure in detail. A series of cavitation models are used in computational fluid dynamics (CFD) simulation to describe the mass transfer of phase change in multiphase flow. The employed simulation methods include potential flow theory (Faltinsen, 2004; Faltinsen and Semenov, 2008), boundary element method (BEM) (Bal, 2007, 2011; Bal and Kinnas, 2002), and large eddy simulation (LES) (Wang et al., 2016a). LES can better simulate unsteady large-scale vortex structure movement. In theory, LES can also accurately predict the characteristics of the transient turbulence and small-scale cloud cavitating flow structure (Yuet al., 2014; Wang and Ostoja-Starzewski, 2007; Li et al., 2015; Huang et al., 2014; Dittakavi et al., 2010; Roohi et al., 2013; Ji et al., 2013; Wu et al., 2015).

Most of the previous research focuses on fully submerged underwater cloud cavitating flow while neglecting the free surface or wall effect. Kunz (Kunz et al., 1999) analyzed natural and ventilated cavitation characteristics around submerged bodies by using multiphase CFD method, which includes surface pressure distribution, cavitation bubble geometry and drag coefficient. Owis (Owis and Nayfeh, 2004) computed three-dimensional (3D) incompressible, multiphase flows over cavitating projectiles with different geometries. Using the open-source software OpenFOAM, Yu (Yuet al., 2014) analyzed the shedding and collapsing phase-changing process of cloud cavitating flow around an axisymmetric projectile, in which the LES methodology is applied to simulate the dynamic behavior of cavitation with the volume of fluid (VOF) method for interface capture and the Kunz model (Kunzet al., 2000) for mass transfer. The evolution of natural cavitation, the formation and development of the re-entrant jet, and the evolution of the shedding bubble are presented in the study.

Free surface near the cavitating flow may affect the cavity profile and evolution. In this topic, most research has focused on steady cavitation, such as supercavitation. Dawson (1959) conducted several early experiments to study the free surface effect on a wedge-shaped supercavitating hydrofoil. A brief view of the cavity evolution, and the center of pressure location, forces, and moment are studied. Other research on the cavitating flow over hydrofoil under the free surface effect was conducted by potential flow theory (Liang et al., 2013; Karim et al., 2014; Xie and Vassalos, 2007). Furthermore, the relationship between the submerged depth and the cavity length is discussed by Franc and Michel by using linearized theory (Franc and Michel, 2004). Faltinsen and Semenov (2008) presented a nonlinear analysis of the supercavitating flow around the hydrofoil beneath the free surface. The free surface effect is substantial. As the submerged depth of the hydrofoil decreases, the cavity on the hydrofoil becomes shorter with an unchanged cavitation number. Wang (Wang et al., 2016a, 2016b) studied the free surface effect on the cloud cavitating flow around an axisymmetric projectile with and without atmospheric ventilation. Strong air entrainment into the cavity on the upper side of the blunt body makes the cavity much larger and more stable. Gnanaskandan (Gnanaskandan and Mahesh, 2015, 2016) used a sensor that can test vapor volume fraction in the experiment. Both Reynolds-averaged Navier–Stokes (RANS) and LES methods are validated based on the experimental data. It was found that the LES results are more accurate than the RANS results for the highly unsteady flow problem.

Studying the characteristics and mechanisms of unsteady cavitating flow around an axisymmetric projectile under the effects of a nearby wall is also quite complex. Ishida and Kimoto (Ishida et al., 2001; KIMOTO et al., 1985) studied single cavitation bubble behavior on a wall and near-wall boundaries using a complex test facility and a high-speed camera for recording. The wall effect on the bubble can be classified by the distance between the walls and the bubble radius. Zhou, Chen G, and Chen X (Chen et al., 2015; Zhou et al., 2010; Xin et al., 2008) conducted water tunnel experiments and numerical calculations of the sheet, cloud, and ventilated cavitating flow under the wall effect. The tracked pressure signal shows that excited pressure fluctuations occur during the process. The length of the super cavity increased with the extent of the blocking effect, whereas its diameter decreased. He and Kida (He et al., 2014; KIDA and MIYAI, 1975; Kida and Miyai, 1972) studied the near-wall effect on supercavitating jet-flapped foils. The cavitating flow is simulated around a hydrofoil with various distances to the sidewall. The significant 3D characteristics and the detailed mechanisms of the natural cavity are studied under the effect of the wall.

However, cavitating flow under the mutual effect of the free surface and wall is only considered in very few studies. Amromin (2007) showed the 3D deformations of the body supercavitation under the mutual effect of free surface and wall. The ideal fluid theory was applied out in the article. Chen (Xin et al., 2011) simulated natural cavitating flows around a 2D wedge in “shallow water”. Under the mutual effect, the observed cavity configurations contain three types: stable, transition, and wake vortex. The shapes of the free surface and the cavity surface, and the hydrodynamic performance of the wedge are also discussed. Most previous studies on cavitation only considered supercavitating flow when the cavitation number is small (about 0.1–0.2). The existing studies on cloud cavitating flow are relatively few and did not consider the mutual effects of the free surface and wall. The mechanism of the free surface and wall effect on the cavitating flow has not been studied.

Bearing this in mind, in this work, we investigated the 3D unsteady cloud cavitating flow at a moderate cavitation number (about 0.5) that surrounds an axisymmetric projectile using the water tank experiment and the numerical approach, with a focus on the mutual effects of the free surface and wall. Split-Hopkinson pressure bar (SHPB) technology is used in the water tank experiment to launch the projectile into the water tank in a short time (in less than 50 μs). The VOF method, LES turbulence model, and Zwart-Gerber-Belamri (ZGB) cavitation model (Zwart et al.,) are applied in the simulation to capture the cavitating flow pattern and the multiphase interfaces (water, vapor, and air) flow. First, the numerical methods are validated and verified against the experimental data. Then, by varying the distances between the projectile and boundaries, the cavitation under different working conditions is analyzed.

The typical cloud cavitating flow over the projectile is shown in Fig. 1. The evolution of the cloud cavitating can be affected by the parameters including the projectile diameter (D), the free stream velocity (U), the distance between the upper surface of the projectile and free surface (d_f), the distance between the lower surface of the projectile and bottom wall (d_w), and the cavity length (l), which are indicated in Fig. 1. Mutual effects of the free surface and bottom wall happen when the boundaries are close to the projectile, which means the depth of the water is comparable to the diameter of the projectile (approximately less

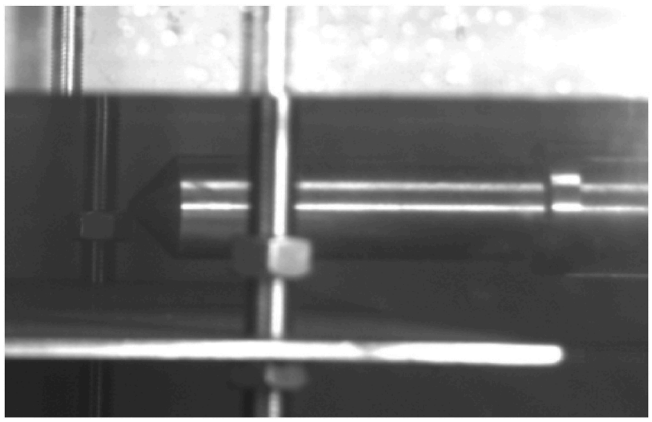

Fig. 2. Water tank test facility.

than three times of the diameter). In this paper, the term "shallow water" is referred to the water depth where such mutual effects apply. It should be noted that this definition of "shallow water" is different from the commonly used definition in the shallow water equation (Whitham, 2011). It can be observed from the experimental results that there are four stages in the cavity evolution, including cavity growth, re-entrant jet, cavity shedding, and collapsing. The free surface/wall can largely affect the characteristics of the cloud cavitating flow, including the cavity profile, period of cavity evolution (T), cavity stability, etc. By placing the projectile near the free surface/wall, the cavity curvature and stability increase as d_f decreases, and decreases as d_w decreases. Under the 3D effect, the interactions of the cavitating flow between the upper and lower sides of the projectile will weaken the mutual effects of free surface and wall. The typical cloud cavitating flow under this mutual effects can be categorized into several distinct flow regimes in the parameter space spanned by d_f/D, and d_w/D contains the entire shedding cavity (symmetry/asymmetry), steady and non-shedding cavity, partial cavity shedding, and ventilated cavity.

Section 1 introduces the full article and presents a literature survey. Section 2 describes the whole water tank experiment system. Section 3 presents the numerical methods, including the governing equations, LES approach, Cartesian cut-cell mesh, numerical setups. Section 4 discusses and presents an analysis of the results. Section 4.1 validates the numerical method and discusses the whole cavity evolution process of a typical case for both the experimental and numerical results. Section 4.2 describes the mutual effects of the free surface and the bottom wall on the cavitating flow. Section 4.3 presents the four distinct flow regimes under the mutual effects. Section 5 offers the concluding remarks.

2. Water tank experiment

A series of water tank experiments are performed to study how the cavitating flow over the projectile changes with d_f and d_w. Experiments are conducted in the water tank at the Key Laboratory for Mechanics in Fluid Solid Coupling Systems at the Institute of Mechanics, Chinese Academy of Sciences. The detailed experimental setups have been described in our previous work (Wang et al., 2016c; Xu et al., 2017), and we only are summarized them here briefly. Fig. 2 shows the water tank test facility. The projectile measures 200 mm × 37 mm × 37 mm is a steel cylinder with a conical head. The water tank is 1 m × 1 m × 2 m. The SHPB technology (Yan-Peng et al., 2011) is used for projectile launching, which can accelerate the model to approximately 20.5 m/s in less than 50 μs with little disturbance to the free surface. When the incident bar hits the transfer bar, a strong stress wave is generated and propagated into the projectile, driving it forward. The distance that the projectile travels during the acceleration is less than 0.03D, while the total travel distance in the first cavity evolution period (about 18 ms) is about 9.97D. Therefore, the disturbance during acceleration can be neglected. A high-speed camera with 25000 FPS (frames per second) is used to record the experiment. The launching process is shown in Fig. 3. The cavitation number is calculated as:

$$\sigma = \frac{p_\infty - p_v}{\frac{1}{2}\rho_l U^2} = 0.47 \tag{1}$$

where $p_\infty = 101.325$ kPa is the standard atmospheric pressure, $p_v = 2450$ Pa is the saturated vapor pressure, $\rho_l = 1000$ kg/m^3 is the water density, and U is the launching speed. We obtained the exact speed value by analyzing the model motion in images, which is approximately constant at 20.5 m/s during the first cavity evolution period.

3. Numerical methods

3.1. LES and VOF approaches

The multiphase flow equation is used to solve the three-phase (water, vapor, and air) flow problem. The Navier-Stokes equations of the incompressible flow by applying the filter function of LES are

$$\frac{\partial \rho}{\partial t} + \frac{\partial\left(\rho \overline{u}_j\right)}{\partial x_j} = 0 \tag{2}$$

$$\frac{\partial\left(\rho \overline{u}_i\right)}{\partial t} + \frac{\partial\left(\rho \overline{u}_i \overline{u}_j\right)}{\partial x_j} = -\frac{\partial \overline{p}}{\partial x_j} + \frac{\partial}{\partial x_j}\left(\mu \frac{\partial \overline{u}_j}{\partial x_j}\right) - \frac{\partial \tau_{ij}}{\partial x_j} \tag{3}$$

where τ_{ij} is the subgrid scale (SGS) stress, which is defined as

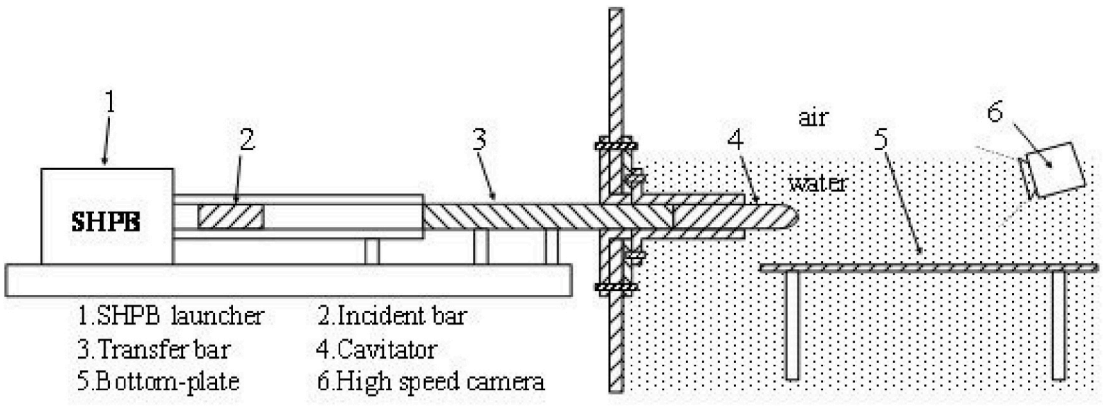

Fig. 3. Schematic of the launching process.

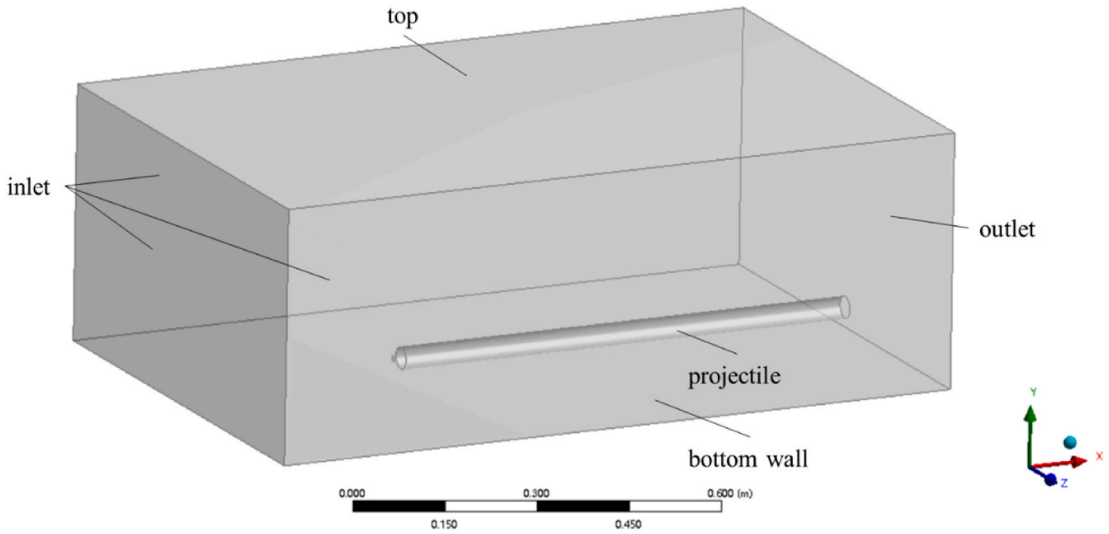

Fig. 4. Computational domain and boundary conditions.

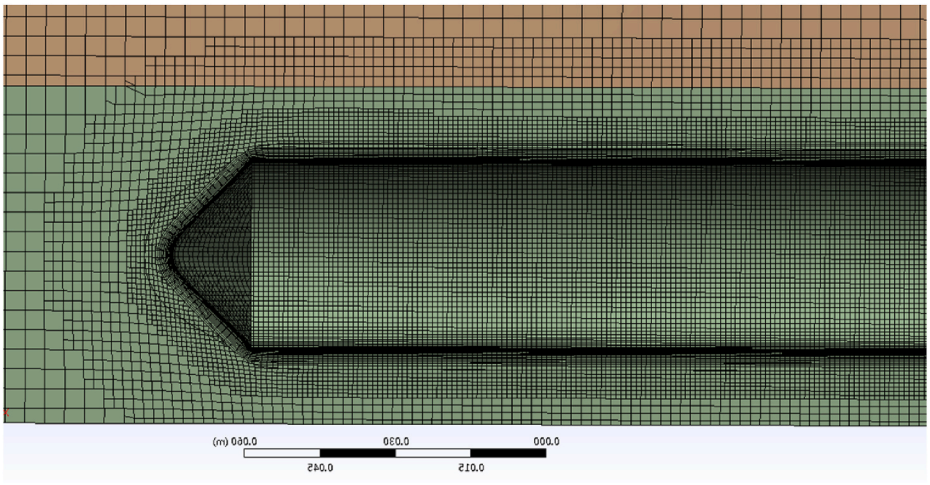

Fig. 5. Cartesian cut-cell mesh around the projectile. The total mesh size is 3.42 million.

$$\tau_{ij} = \rho\left(\overline{u_i u_j} - \overline{u}_i \overline{u}_j\right) \tag{4}$$

Based on the Boussinesq equation, the SGS stress can be computed from

$$\tau_{ij} - \frac{1}{3}\tau_{kk}\delta_{ij} = -2\mu_t \overline{S}_{ij} \tag{5}$$

where μ_t is the SGS turbulent viscosity, τ_{kk} is the isotropic part, and $\overline{S}_{ij}$ is the rate of strain, which is defined as

$$\overline{S}_{ij} \equiv \frac{1}{2}\left(\frac{\partial \overline{u}_i}{\partial x_j} + \frac{\partial \overline{u}_j}{\partial x_i}\right) \tag{6}$$

In the wall-adapting local-eddy viscosity (WALE) model, the eddy viscosity is modeled by

$$\mu_t = \rho \Delta_s^2 \frac{\left(S_{ij}^d S_{ij}^d\right)^{3/2}}{\left(\overline{S}_{ij}\overline{S}_{ij}\right)^{5/2} + \left(S_{ij}^d S_{ij}^d\right)^{5/4}} \tag{7}$$

where $\Delta_s = C_w V^{1/3}$, $S^d{}_{ij} = \frac{1}{2}(\overline{g}^2{}_{ij} + \overline{g}^2{}_{ij}) - \frac{1}{3}\delta_{ij}\overline{g}^2{}_{kk}$, $\overline{g}_{ij} = \frac{\partial \overline{u}_i}{\partial x_j}$, and $C_w = 0.325$ is the constant.

ρ, p and μ are the density, pressure and viscosity of the mixture, which are

$$\mu = (1 - \alpha_v - \alpha_a)\mu_l + \alpha_v \mu_v + \alpha_a \mu_a \tag{8}$$

$$\rho = (1 - \alpha_v - \alpha_a)\rho_l + \alpha_v \rho_v + \alpha_a \rho_a \tag{9}$$

where α is the volume fraction of the different phases a, l and v represent air, liquid water and water vapor, respectively. The $\rho_l = 998.2\ kg/m^3$, $\rho_v = 0.5542\ kg/m^3$ and $\rho_a = 1.225\ kg/m^3$ are constant. Now the unknowns become α_a and α_v. By using the VOF method, the equation set is closed by the transport equations

$$\frac{\partial(\alpha_a \rho_a)}{\partial t} + \frac{\partial(\alpha_a \rho_a u_j)}{\partial x_j} = 0 \tag{10}$$

$$\frac{\partial(\alpha_v \rho_v)}{\partial t} + \frac{\partial(\alpha_v \rho_v u_j)}{\partial x_j} = \dot{m}^+ - \dot{m}^- \tag{11}$$

where $\dot{m}^+$ and $\dot{m}^-$ are the mass transfer rate of evaporation and condensation, derived from the Rayleigh–Plesset bubble dynamics equations presented by Zwart et al..

Table 1
Numerical schemes and parameters.

Scheme in time	Second-order implicit
Pressure interpolation	Body Force Weighted
Scheme in volume fraction	Modified HRIC
Inlet velocity	20.5 m/s
Time step size	1×10^{-5}s

$$\dot{m}^{+} = F_{vap}\frac{3a_{nuc}(1-\alpha_v)\rho_v}{R_B}\sqrt{\frac{2}{3}\frac{max(p_v-p,0)}{\rho_l}} \tag{12}$$

$$\dot{m}^{-} = F_{cond}\frac{3\alpha_v\rho_v}{R_B}\sqrt{\frac{2}{3}\frac{max(p-p_v,0)}{\rho_l}} \tag{13}$$

where $R_B = 10^{-6}\ m$ is the generalized bubble radius, $p_v = 2340$ Pa is the saturated vapor pressure, $a_{nuc} = 5 \times 10^{-4}$ is the nucleation site volume fraction, $F_{vap} = 50$ is the evaporation coefficient, and $F_{cond} =$

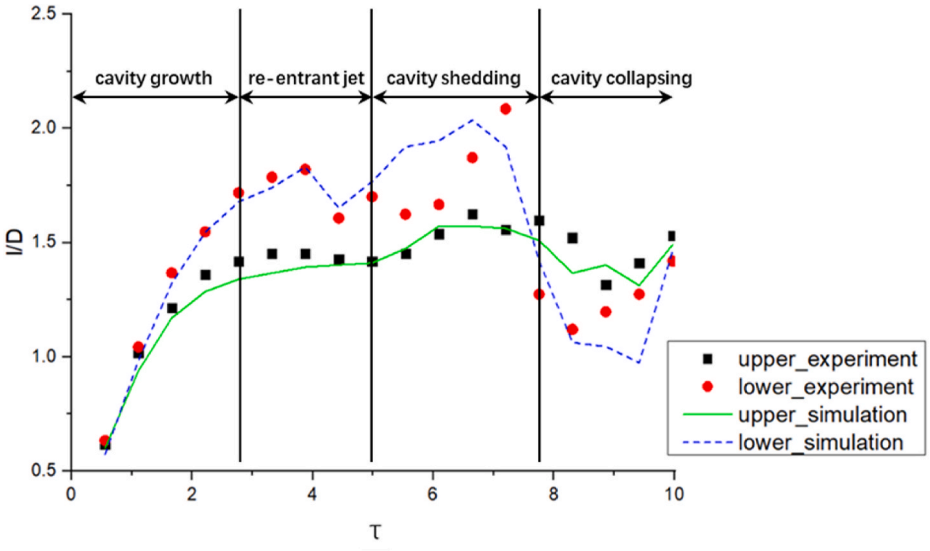

Fig. 6. Comparison between experimental and simulation results of the dimensionless cavity length l/D on the upper and lower sides of the projectile at the dimensionless time τ when the dimensionless distance between the projectile and the free surface/bottom wall is $d_f/D = d_w/D = 0.405$.

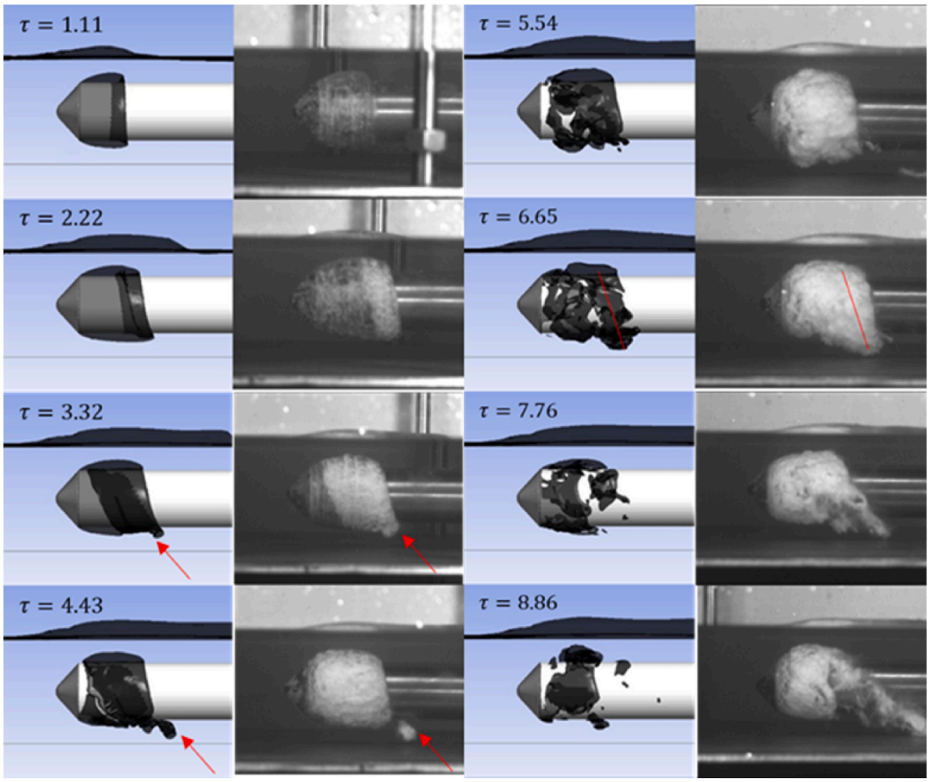

Fig. 7. Comparison of the cavity patterns between experiment and simulation results.

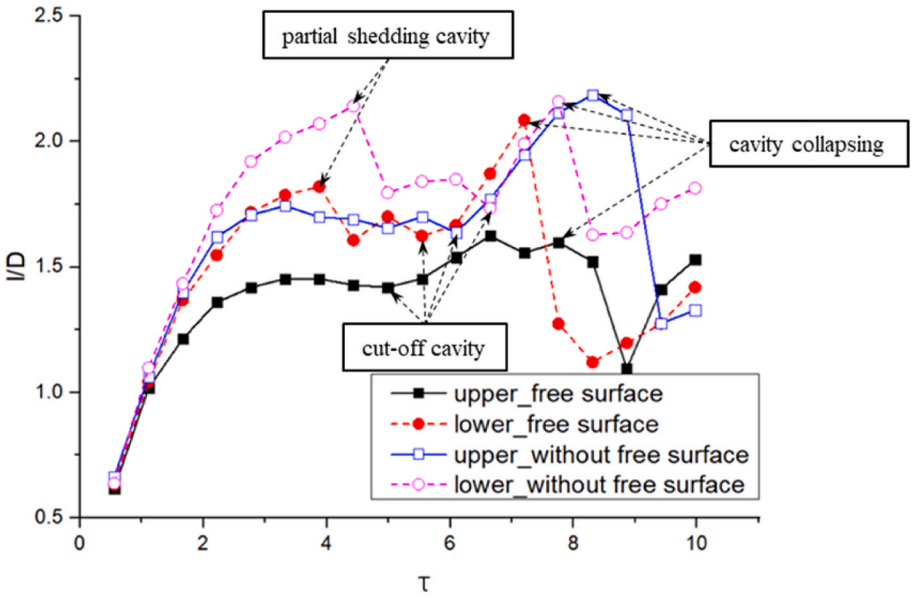

Fig. 8. Velocity contour charts show the velocity distribution changes around the projectile from $\tau = 2.22$ to $\tau = 4.99$. The forming partial cavity shedding on the lower side of the projectile is indicated by red arrows. (For interpretation of the references to colour in this figure legend, the reader is referred to the Web version of this article.)

0.01 is the condensation coefficient. The chosen parameter values have been discussed and found to work well for various fluids and devices (Wang et al., 2016a).

3.2. Simulation setups

In this study, the commercial software ANSYS Fluent is used to simulate the cavitating flow over an axisymmetric projectile under the mutual influence of the free surface and the bottom wall. Fig. 4 shows the calculation domain and boundary conditions, including velocity inlet, pressure outlet, projectile (no-slip wall), and bottom wall. By ignoring the influence of the tail, the simulation uses a semi-infinite projectile model. In the simulation, a Cartesian cut-cell mesh plan with 15 layers of inflation is used. The height of the first layer is set to 1×10^{-4} m, and the growth rate is 1.1 (as shown in Fig. 5). The total number of cells is about 3.42 million, which has good orthogonality.

LES and the WALE model are adopted to simulate the turbulent flow. Other detailed numerical schemes and parameters are listed in Table 1. Second-order implicit scheme is used for time discretization of the volume fraction equation, which is compatible with the cavitation model. The modified high-resolution interface-capturing (HRIC) scheme (Muzaferija, 1999) is also used in volume fraction. The body force weighted is applied for pressure interpolation. Given that the whole acceleration process is very short in the experiment, the unsteady cavitating flow simulations start from a uniform flow field. The time step size is set as 10^{-5}s.

4. Results and discussion

4.1. Comparison of cavity evolution process

The dimensionless cavity length (l/D) that grows with dimensionless time ($\tau = tU/D$) on the upper and lower sides of the projectile from the experiment and simulation results are compared in Fig. 6. The distance between the projectile and the free surface/bottom wall is $d_f/D = d_w/D = 0.405$. The cavity length is measured from images of experimental and simulation data. The precision of the length measurement is within one image pixel, which corresponds to 0.74 mm on the physical model. The comparison shows that the numerical method is reasonably accurate with a small discrepancy in the cavity shedding on the lower surface, which validate the numerical method used in the simulation. The results show that the cavity evolution includes four stages indicated in Fig. 6: cavity growth, re-entrant jet, cavity shedding, and collapsing. The criteria for defining the stages is based on the work by Wang (Wang et al., 2016a). Fig. 7 to Fig. 10 show the cavity shapes in different stages. The iso-surface of the water volume fraction $\alpha_l = 0.5$ is used to visualize the shape of the cavity of the simulation results.

The typical cavity structure in the cavity growth stage ($\tau = 0$ to 2.77) is shown in Fig. 7, the cavity length grows with time. The cavity has an asymmetric structure with a longer cavity length on the lower side than on the upper side. The difference in the cavity length between the upper and lower sides increases over time as shown in Fig. 6. The height of the free surface varies with the cavity thickness on the upper side of the model.

In the next stage shown in Fig. 7 ($\tau = 2.77$ to 4.99), the white foam like re-entrant jet (shown in the experimental results) appears inside the cavity and moves forward to the leading edge of the cavitating flow. When the re-entrant jet reaches the shoulder of the projectile, it will cut off the cavity by interacting with the outer flow region. The total cavity shape remains nearly unchanged during this time. The re-entrant jet inside the upper cavity reaches the shoulder of the projectile earlier than the lower side. The partial cavity shedding indicated by red arrows can be observed. The cavity on the upper side of the model is shorter and thicker, which means that the curvature of the upper-side cavity is larger, vice versa. Re-entrant jet is important for cavity sheds. The detailed mechanism of the free surface and near-wall effects on the cavity profile and the re-entrant jet inside the cavity that induce instability are discussed in Section 4.2.

The cavity evolution process and the velocity contour show the velocity distribution changes around the projectile over time from $\tau = 2.22$ to 4.99 are shown in Fig. 8. Red arrows indicate the re-entrant jet on the upper and lower sides in the cavity. Compared with the re-entrant jet on the upper side, near the free surface, the re-entrant jet on the lower side is much thicker. The re-entrant jet on the lower side of the projectile beneath the cavitating flow will cut off the cavity by interfering with the main flow outside. Then, partial cavity shedding begins.

In the cavity shedding stage shown in Fig. 7 ($\tau = 4.99$ to 7.76), the cavity generated in the first stage begins to shed, and the new cavity

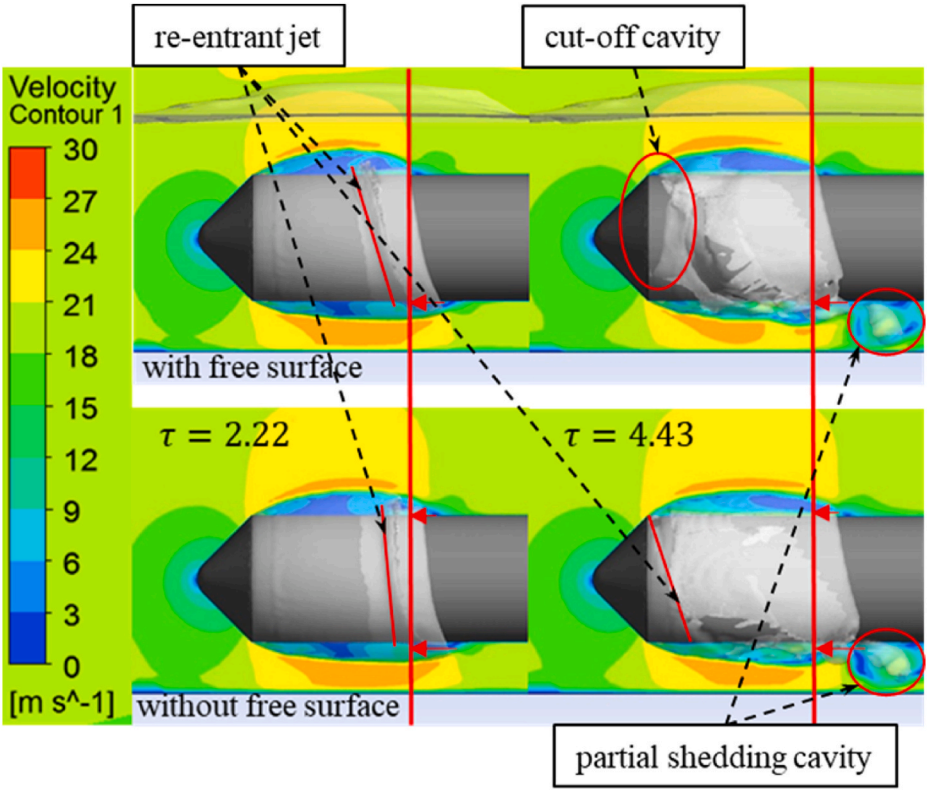

Fig. 9. Comparison of the dimensionless upper- and lower-side cavity length in the water tank experimental results of the tested projectile in "shallow water" and near the bottom wall only when d_f/D and d_w/D is 0.405.

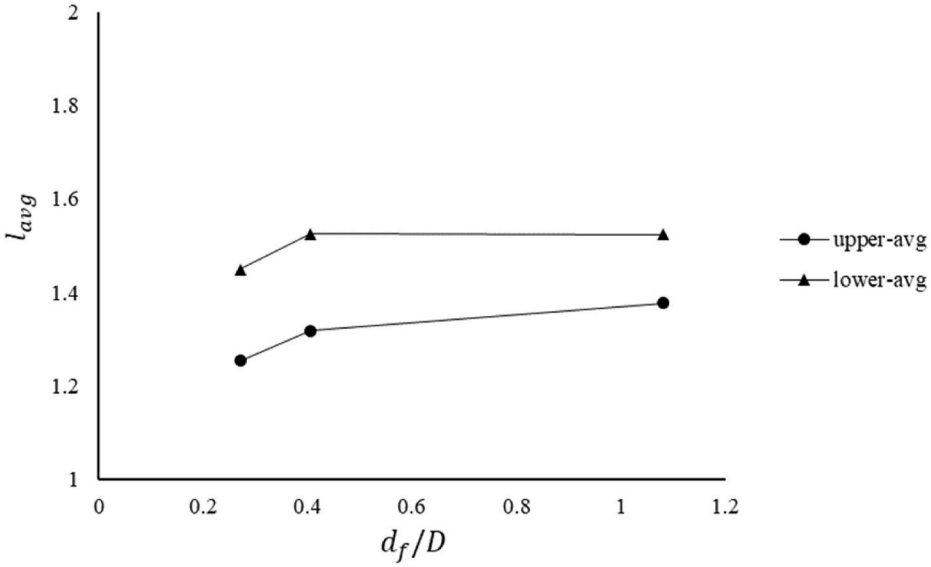

Fig. 10. Comparison of the simulation results with and without free surface at $\tau = 2.22$ and $\tau = 4.43$ (velocity contour charts show the velocity distribution around the model at the added symmetry plane). The differences in the upper and lower cavity length is indicated by red arrows. Typical phenomenon are indicated by black arrows. (For interpretation of the references to colour in this figure legend, the reader is referred to the Web version of this article.)

grows. The overall length of the cavitating flow becomes much longer than in the previous stages.

The cavity collapses in the last stage shown in Fig. 7 at ($\tau =$ 7.76 to 9.97). As the shedding cavity flows downstream, its concomitant vortex becomes weaker. The cavity at the lower side of the projectile near the wall collapses first. A newly generated cavity grows in the next cavity evolution period. In this study, we only focus on the cavity evolution for the first period.

4.2. Free surface and near-wall effects on cloud cavitating flow

4.2.1. Free surface effect on cloud cavitating flow

To analyze the free surface effect on the cloud cavitating flow around the projectile tested in the water tank experiment, we plot the upper- and lower-side cavity lengths of the experimental results. A comparison between the cases with the projectile in "shallow water" and near the bottom wall are presented in Fig. 9. The cavity evolutions in the two

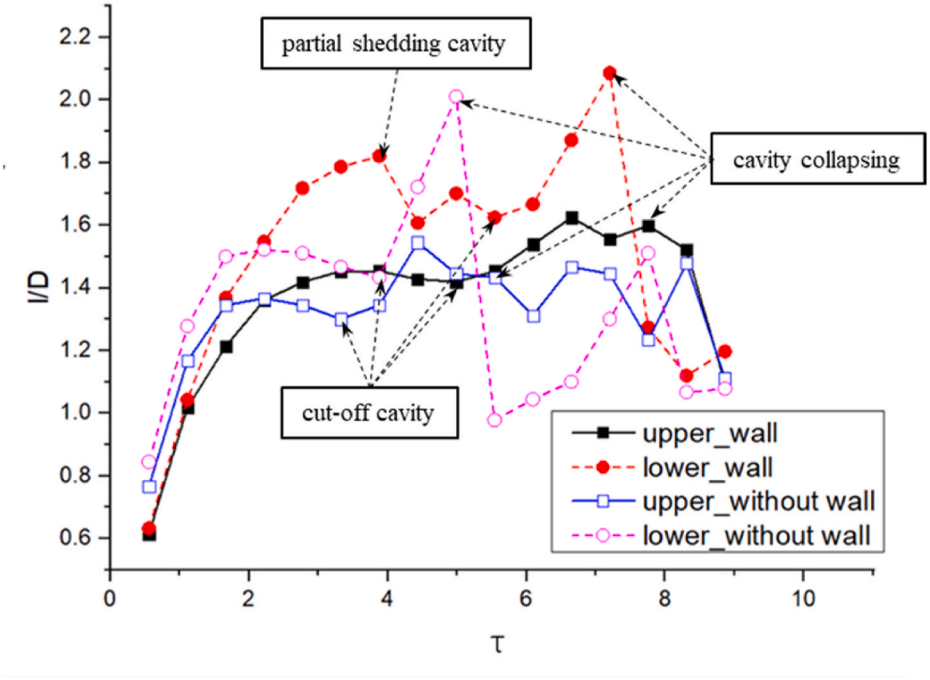

Fig. 11. Time-averaged cavity length on the upper and lower sides of the projectile varies with d_f/D when $d_w/D = 0.405$.

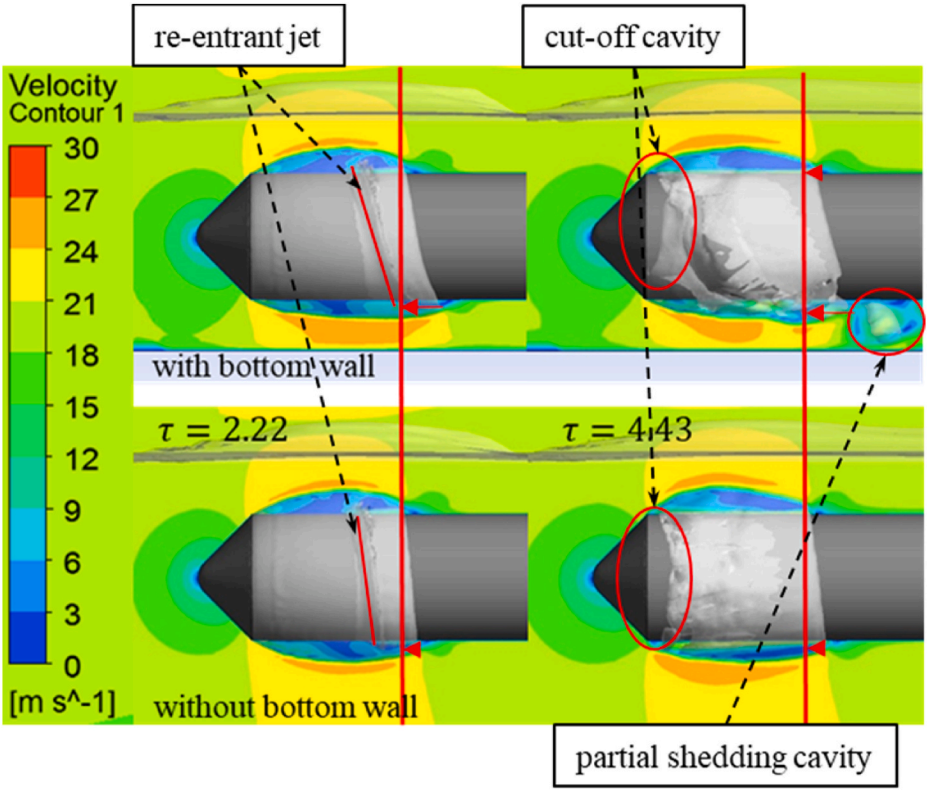

Fig. 12. Comparison of the upper- and lower-side cavity lengths in the water tank experimental results of the tested projectile in "shallow water" and near the free surface only when d_f/D and d_w/D is 0.405.

cases are generally similar. However, it shows that the free surface can induce a shorter l, and shorten the cycle. The time when the typical phenomenon occurs is marked in Fig. 9. The cavity is much more stable in the case with free surface nearby than the case without free surface since the variation of the cavity length is clearly much less when the projectile is near the free surface. Thus, in terms of cavity stability, the free surface have "positive" effects on high-speed cruising in a certain depth range and operating conditions. When the model is placed near the free surface/wall, the new constraints will change the dynamic pressure and the momentum of the incoming flow. Thus, we need to

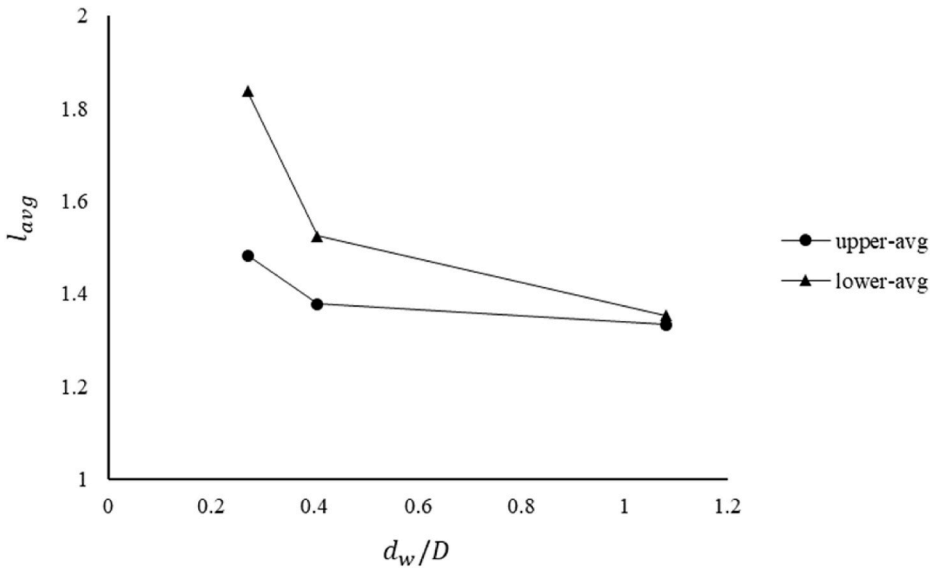

Fig. 13. Comparison of the simulation results with and without bottom wall at $\tau = 2.22$ and $\tau = 4.43$ (velocity contour charts show the velocity distribution around the model at the added symmetry plane). The differences in the upper and lower cavity length is indicated by red arrows. Typical phenomenon are indicated by black arrows. (For interpretation of the references to colour in this figure legend, the reader is referred to the Web version of this article.)

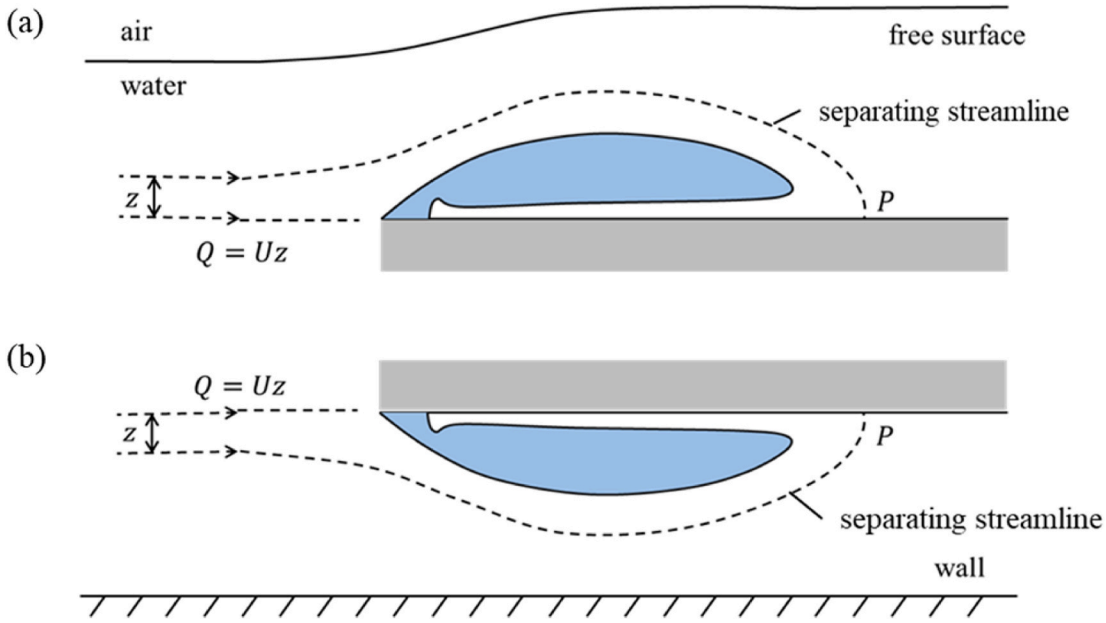

Fig. 14. Time-averaged cavity length on the upper and lower sides of the projectile varies with d_w/D when $d_f/D = 0.405$.

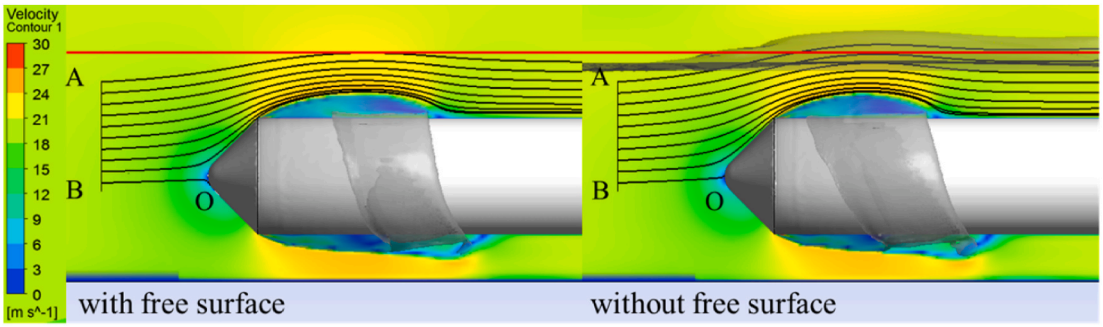

Fig. 15. Schematic interpretation of the stream tube of the re-entrant jet flows towards the head of the model (exaggerated and not to scale) under the (a) free surface effect, (b) near-wall effect.

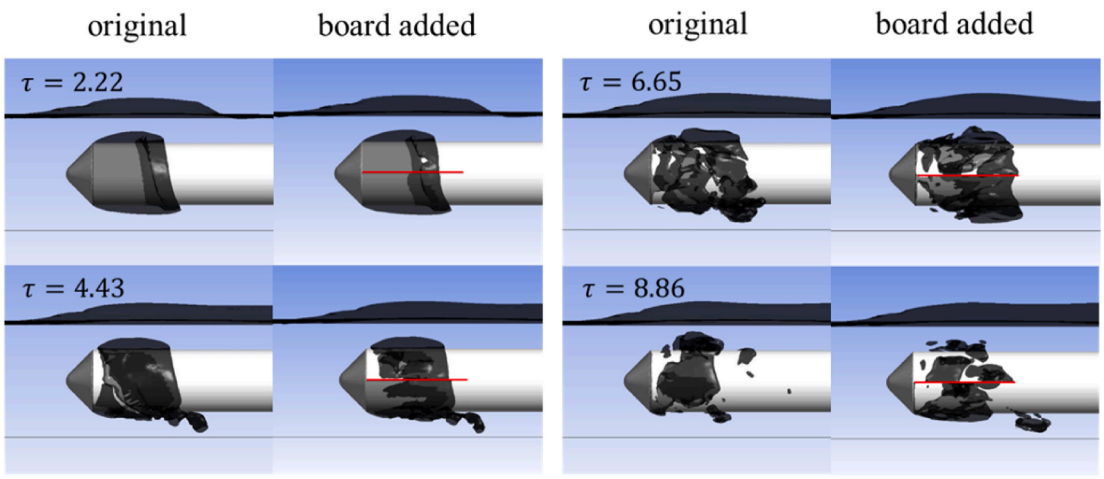

Fig. 16. Comparison of simulated cases with and without free surface. The equally distributed 10 stream lines starting from the added line on the mid-plane from A (-0.05, 0.03) to B (-0.05, −0.004). The reference point O (0, 0) is defined in Fig. 1. $\tau = 3.32$. The added red line indicates the difference in the stream lines. (For interpretation of the references to colour in this figure legend, the reader is referred to the Web version of this article.)

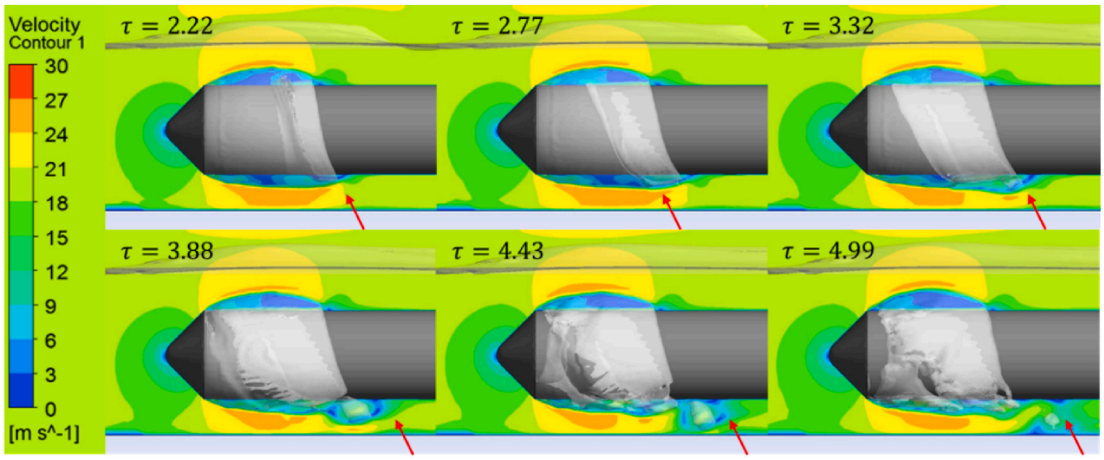

Fig. 17. Comparison of the original simulation results and the simulation results of the case with a non-thickness board (indicate by red lines) added in the middle of the projectile on the Y–Z plane at $\tau = 2.22$, $\tau = 4.43$, $\tau = 6.65$ and $\tau = 8.86$ when d_f/D and d_w/D is 0.405. (For interpretation of the references to colour in this figure legend, the reader is referred to the Web version of this article.)

introduce new parameters: the distance between the upper side of the projectile and the free surface (d_f) and the distance between the lower side of the projectile and the bottom wall (d_w) to study the effects of the free surface/wall.

Fig. 10 shows the simulation results for the cases with/without free surface. The differences in the cavity lengths on the upper and lower side cavity can be observed. Partial shedding cavity occurs in each cases and the free surface near the cavitating flow advance the cavity shedding. The time-averaged cavity length (l_{avg}) when d_f/D varies from 0.27 to 1.08 is plotted in Fig. 11, which shows that will slightly increase with the submerged depth. The changes in cavity profile are caused by the change in the average dynamic pressure ($^1/_2\rho U^2$) of the fluid above the projectile. The velocity of the incoming flow is fixed. When the projectile keeps moving closer to the free surface, the average density of the fluid (we may consider it as a mixture of water and air) above the model will drop significantly, resulting in a drop in average dynamic pressure. From the local cavitation number σ_{loc} (defined in Eq. (1)), the decrease of dynamic pressure will lead to an increase of the σ_{loc}. Then the increased σ_{loc} further leads to the change of cavity profile and affects the cloud cavitating flow characteristics. Thus, the results show that the cavity curvature will become larger, and l will become longer as d_f decreases, and the free surface effect on the cloud cavitating flow will shorten the cycle.

4.2.2. *Near-wall effect on cloud cavitating flow*

Fig. 12 shows a comparison of the upper- and lower-side cavity lengths in the water tank experimental results of the tested projectile in "shallow water" and near the free surface only without a bottom wall nearby. Generally, the overall cavity evolution process for the two cases is similar. The cavity on the upper side is stable during this time. A longer l and T under the near-wall effect for the lower-side cavity are shown in the results. The partial cavity shedding is not shown in the no-wall case, which means that the re-entrant jet thickness λ is not thick enough to cut the cavity, as discussed in Section 4.1.

Fig. 13 presents the simulated results for the cases with/without the bottom wall at $\tau = 2.22$ and $\tau = 4.43$, which shows the differences in the cavity length for the upper and lower side cavity. The time-averaged cavity length (l_{avg}) at d_w/D varies from 0.27 to 1.08 is plotted in Fig. 14, which shows that the wall nearby will cause a drastic change in l_{avg}. The longer cavity induced by the bottom wall compared to the no-wall case is caused by the change in fluid dynamic pressure. With the presence of the bottom wall, the flow flowing through the lower side of the projectile and the wall will become faster (also can be observed in Fig. 13), so the dynamic pressure increases. At the same time, the lower

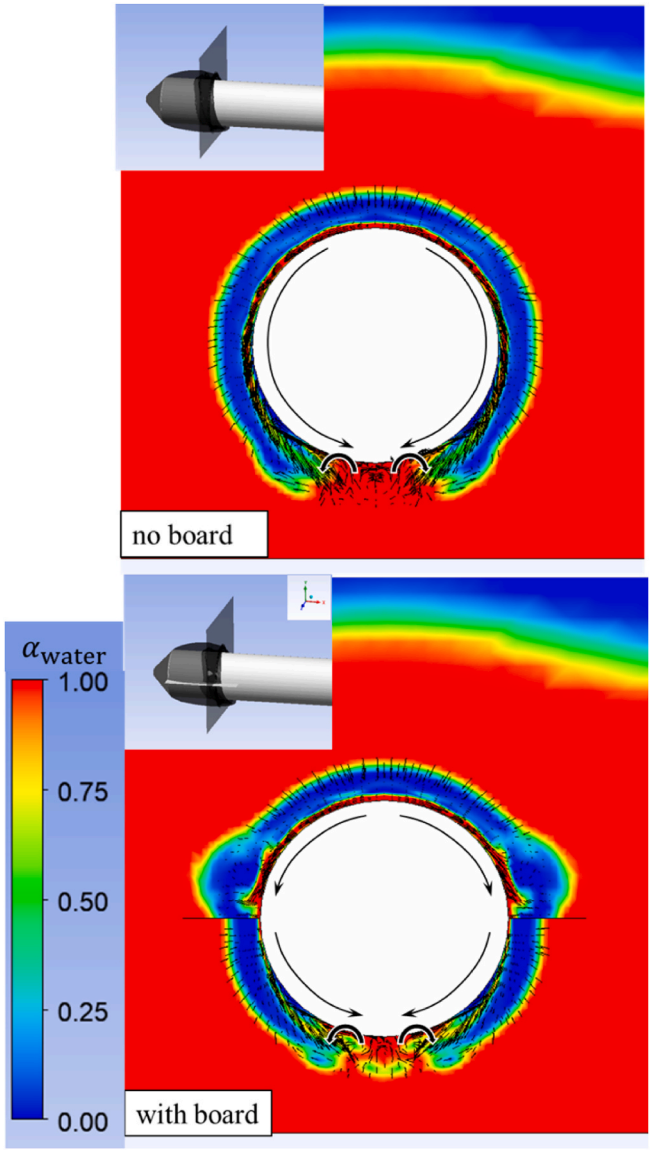

Fig. 18. The velocity vectors in the cross section of the simulated cases with/without the no-thick board at $\tau = 4.43$. The position of the axial slice is 0.925D from the shoulder of the projectile shown in the figure in the upper left corner. The black arrows indicate the direction of the re-entrant jet beneath the cavity.

pressure region between the lower side of the projectile and the bottom lead to a smaller pressure difference between the inside and outside the cavity (i.e., the static pressure in the nominator of Equation (1) decreases). Based on the definition of σ, a lower pressure difference and a higher dynamic pressure lead to a smaller local σ. Thus, l will be longer, the cavity curvature will be larger as d_w decreases, and the cycle increases.

4.2.3. Mechanism of the free surface and near-wall effect on the cavitating flow

Cavitation numberreflects the characteristics of the cavity, which is defined in Eq. (1). Fig. 15 show the schematic of the 'separating streamline" of the re-entrant jet flows towards the head of the model on the upper and lower surfaces. $Q = Uz$ is the re-entrant jet flow rate, U is the free stream velocity, z is the height of the stream tube, where P is the separation point.

For a cavitating model under the free surface effect, the water layer between the free surface and the upper side of the projectile becomes thinner as d_f decreases. So the momentum of incoming flow above the model will reduce. In the case without the free surface, some of the streamlines in the re-entrant jet stream tube will leave the tube and continue to flow downstream under the free surface effect (shown in Fig. 16, comparison of the streamlines between the cases with and without free surface), which means that Q will reduce (z will also reduce as U remains constant) and the separation point P will move towards the head of the projectile. Thus, the reduction of Q leads to a tinner re-entrant jet inside the cavity as d_f decreases. As the re-entrant jet thickness λ decreases, the cloud cavitating flow will become more stable.

Next, we continue to discuss the near-wall effect on the re-entrant jet inside the cavity. Fig. 15 shows the schematic of the stream tube of the re-entrant jet for the case with the bottom wall. As a "strong" constraint, the bottom wall near the projectile will exert an upward momentum on the flow flowing between the lower side of the projectile and the bottom wall. The upward momentum exerted by the bottom wall will shift the direction of the velocity of the flow upward. Some of the streamlines flow downstream will enter the stream tube of the re-entrant jet. In this case, Q will increase (z will also increase as U remains constant), and the separation point P will move away from the head of the projectile. So, under the near-wall effect, λ increases as d_w decreases. The cloud cavitating flow will become less stable with a thicker re-entrant jet inside the cavity.

4.2.4. Interaction inside the cavity

To further study the 3D effect on the cloud cavitating flow, a board without thickness is added on the Y–Z plane to reduce the interaction between the cavity on the upper and lower sides of the projectile. Fig. 17 shows the result comparison between the original case and the case with the additional board. The most obvious difference occurs at $\tau = 4.43$ when partial cavity shedding occurs. For the case without the non-thickness board, the entire cavity sheds on the upper and lower sides of the projectile. However, for the case with the board, the cavity on the lower side of the projectile does not shed at the shoulder, which means the lower side cavity shedding is delayed by the board. The results of the flow velocity vector in Fig. 18 shows that the re-entrant jet moves obliquely downward and converges at the downside of the projectile. As the non-thickness board holds back the interaction of the upper and lower side jet beneath the cavity, the shedding of the cavity is delayed. A pair of vortex sheds with the partial shedding cavity, and induce velocity of the vortex shown in the simulation results. The results indicate that the interaction inside the cavity under the 3D effect will weaken both the free surface and wall effect on the cloud cavitating flow.

4.2.5. Effects on shedding vortex structures

The relationship between the shedding cavity and the vortex motion can be visualized based on the Q criterion (Sahner et al., 2005), which is defined by the following equation in incompressible flow:

$$Q = \frac{1}{2}\left(\Omega^2 - D^2\right) \tag{14}$$

where $\Omega = \frac{1}{2}(\nabla\vec{v} - \nabla\vec{v}^T)$ is the vorticity tensor, and $D = \frac{1}{2}(\nabla\vec{v} + \nabla\vec{v}^T)$ is the strain rate tensor. In addition, Q has a direct physical interpretation, where $Q > 0$, and vorticity dominates strain. Thus, Hunt (1987) identified vortex regions with $Q > 0$.

Fig. 19 presents the velocity distribution on the added iso-surface of $Q = 50000$ at $\tau = 5.54$, $\tau = 6.65$, $\tau = 7.76$, and $\tau = 8.86$ for the simulation cases in "shallow water" (d_f/D and d_w/D are 0.405), near the free surface only, and near the wall only. The results contain the cavity shedding and collapsing stages. Comparing Figs. 7 and 19, cavity evolution strongly correlates with the vortex structure. Aside from the non-axisymmetric broken vortex around the hydrofoil, the results also show the free surface and bottom wall effects on the broken vortex structures. Significant differences occur near the bottom wall. The effect of the bottom wall promotes a large vortex broken into small ones. The shedding vortex breaks up, which is strongly induced by the collapse of the

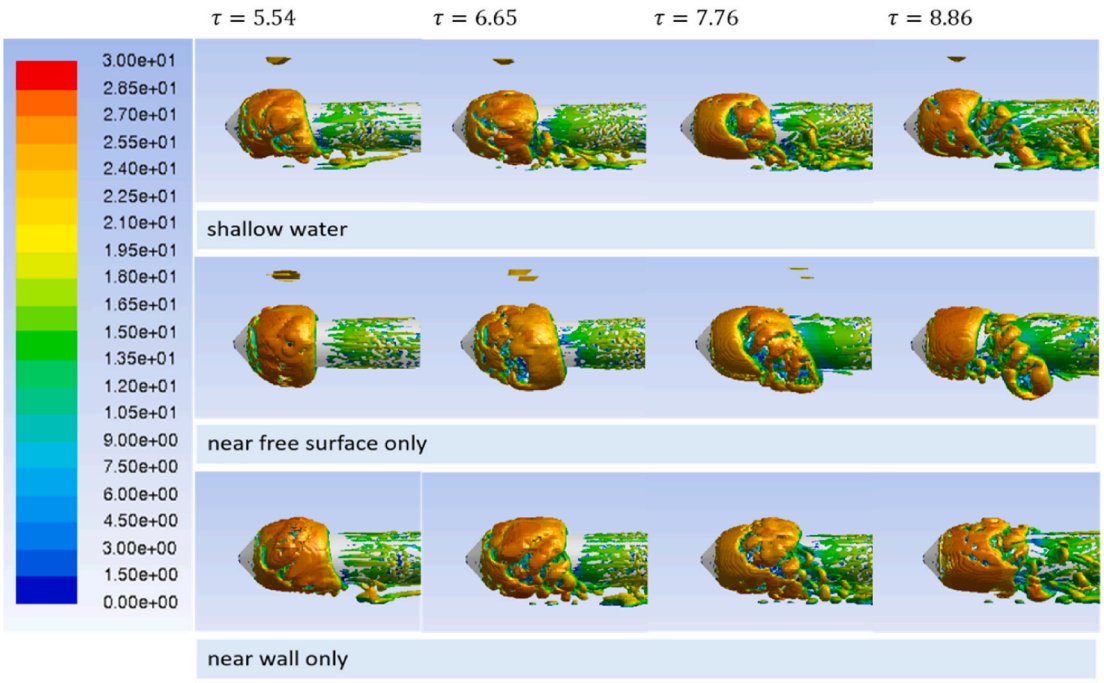

Fig. 19. Velocity distribution on the added iso-surface of $Q = 50000$ at $\tau = 5.54$, $\tau = 6.65$, $\tau = 7.76$, and $\tau = 8.86$ of the simulated cases in "shallow water", near the free surface only, and near the wall only when d_f/D and d_w/D is 0.405.

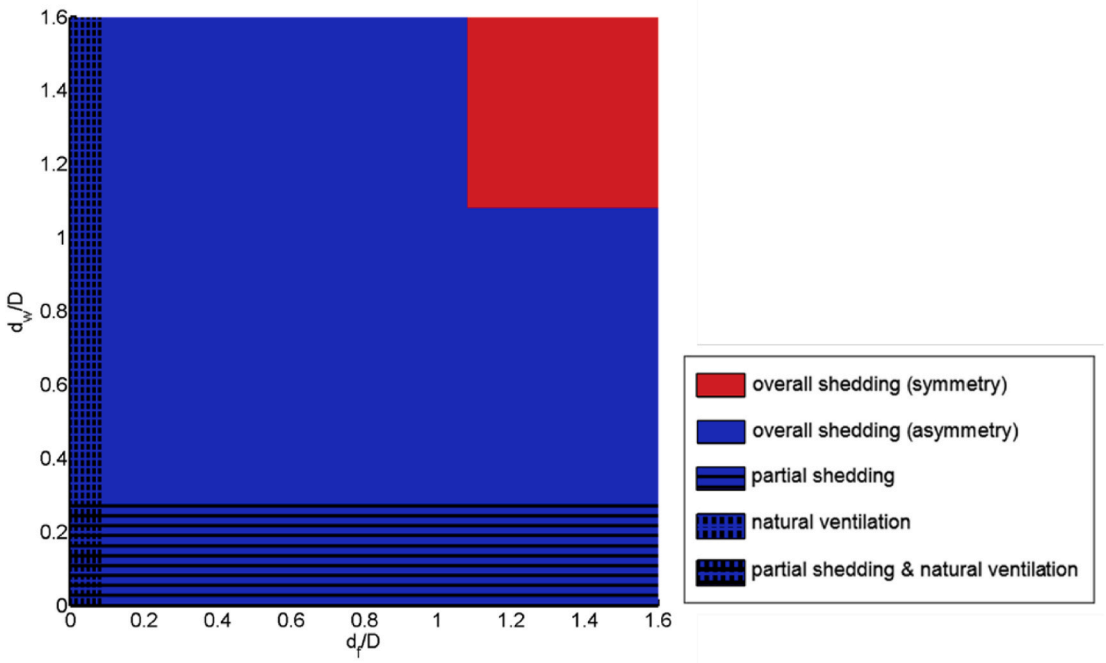

Fig. 20. Dominant cavity profile in different flow regimes as a function of d_f/D and d_w/D at a fixed cavitation number of $\sigma = 0.47$. Shedding regions indicate experimentally observed regime boundaries that contain the symmetrical and asymmetrical overall shedding cavities. Overlapping zones are denoted by hatching, which include the partial cavity shedding, natural ventilation, and the region where cavity partial shedding and natural ventilation occur.

shedding cavity that is much thicker on the lower side of the projectile in the case without the bottom wall nearby. For the simulation cases near the wall, numerous small disturbances that move downstream between the lower side of the projectile and the wall can be observed. The effect of the free surface appears at $\tau = 7.76$. Furthermore, no apparent fracture on the upper-side cavity is observed near the free surface.

4.3. Dominant cavity profile in different flow regimes

The cavity profile exhibits very different structures in the parameter space spanned by d_f/D and d_w/D. In this parameter space, five distinct flow regimes can be identified including the entire shedding cavity (symmetry/asymmetry), steady and non-shedding cavity, partial cavity shedding, and ventilated cavity. Shown in Fig. 20 at a fixed cavitation

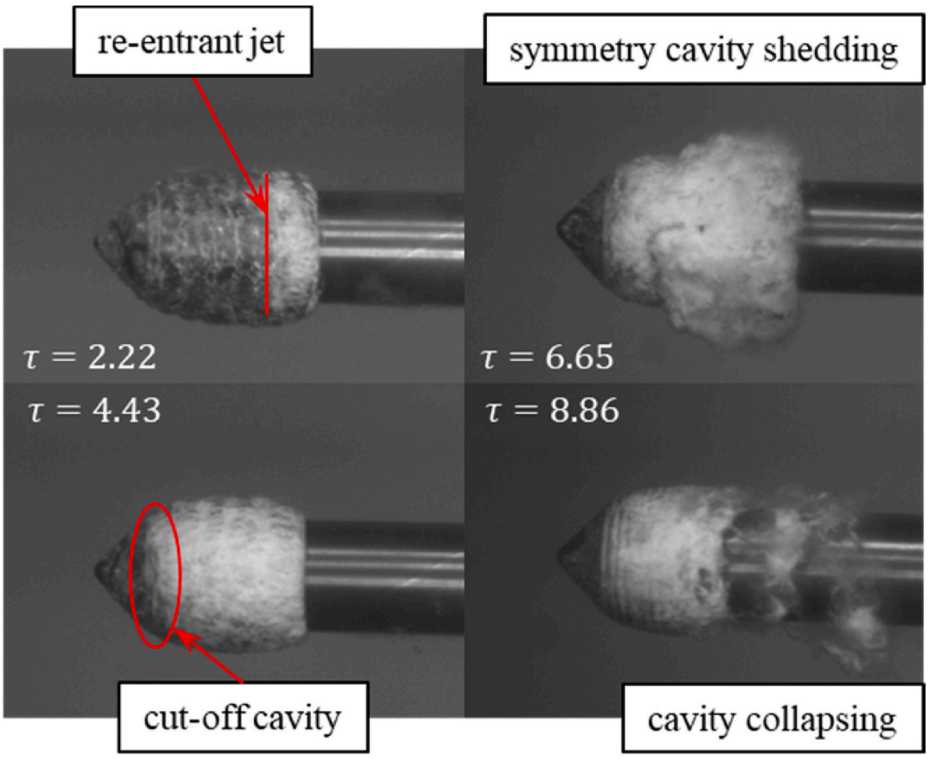

Fig. 21. Typical cavitating flow around the underwater launched projectile at $\tau = 2.22,\ 4.43,\ 6.65$ and 8.86 in deep water. Typical phenomenon are indicated by red arrows in the figure. (For interpretation of the references to colour in this figure legend, the reader is referred to the Web version of this article.)

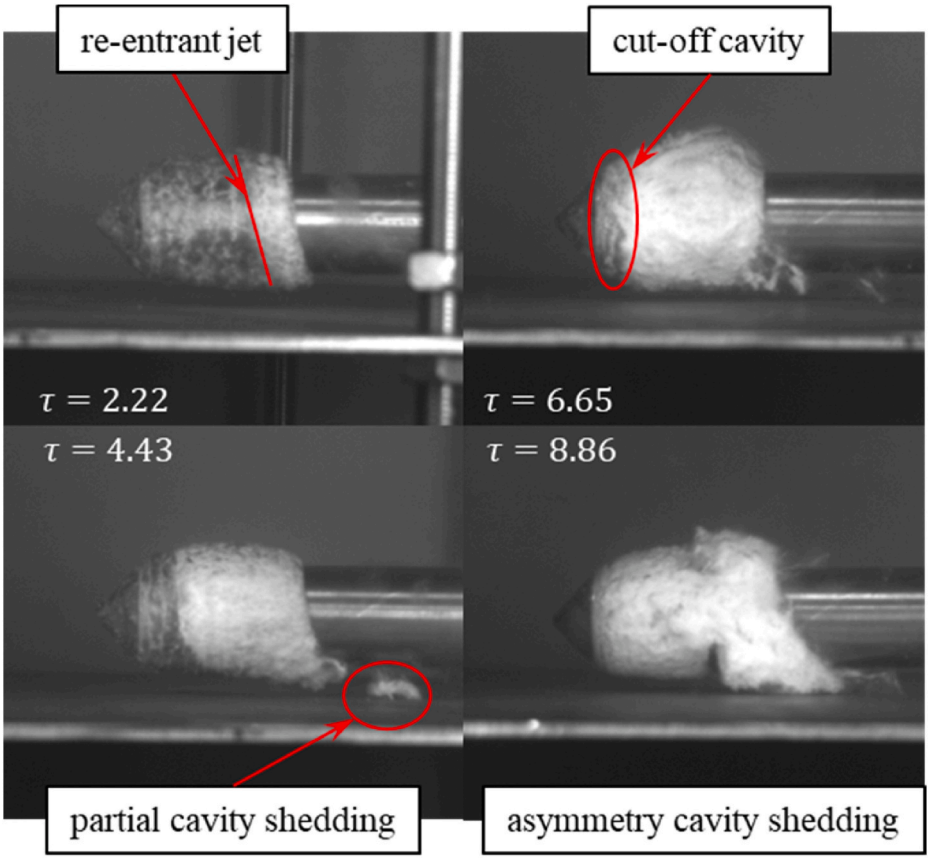

Fig. 22. Typical cavitating flow around the underwater launched projectile at $\tau = 2.22,\ 4.43,\ 6.65$ and 8.86 when $d_w/D = 0.270$. Typical phenomenon are indicated by red arrows in the figure. (For interpretation of the references to colour in this figure legend, the reader is referred to the Web version of this article.)

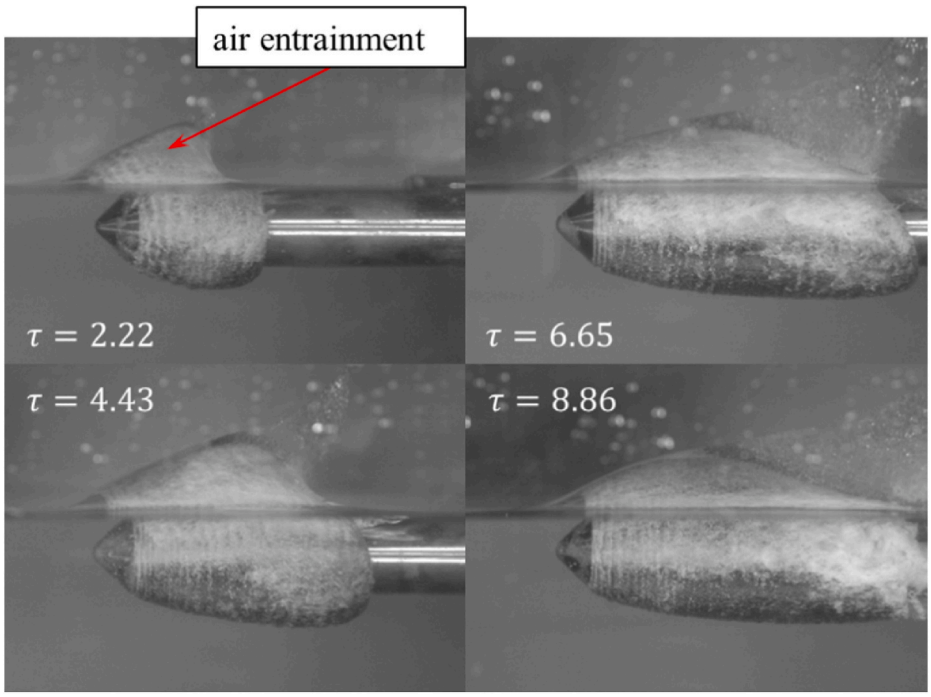

Fig. 23. Typical cavitating flow around the underwater launched projectile at $\tau = 2.22,\ 4.43,\ 6.65$ and 8.86 when d_f/D is 0. Furthermore, air entrainment occurs. Typical phenomenon is indicated by red arrows in the figure. (For interpretation of the references to colour in this figure legend, the reader is referred to the Web version of this article.)

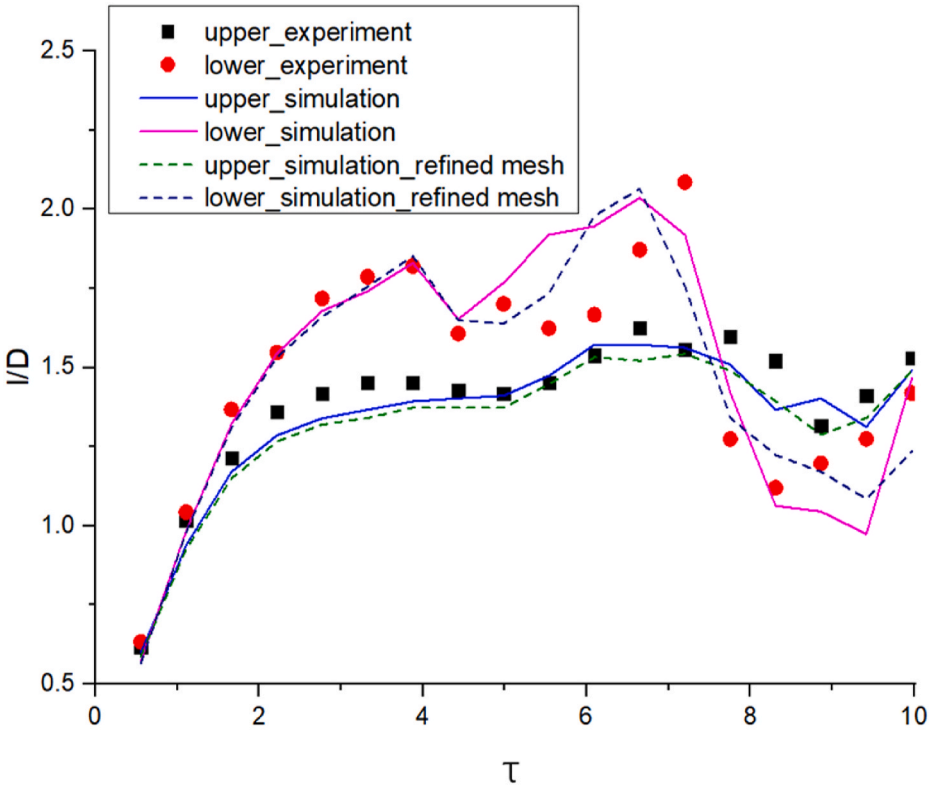

Fig. 24. Comparison between experimental, original mesh, and refined mesh simulation results of the dimensionless cavity length l/D on the upper and lower sides of the projectile at the dimensionless time τ when $d_f/D = d_w/D = 0.405$.

number of $\sigma = 0.47$. The typical phenomenon are listed.

Fig. 21 shows the typical cloud cavitating flow over a projectile launched in deep water. The experimental data shows the symmetry cavity profile during the evolution and the entire shedding cavity. The asymmetry cloud cavitating flow can be observed around the projectile in "shallow water" when d_f/D and d_w/D are less than about 1.081.

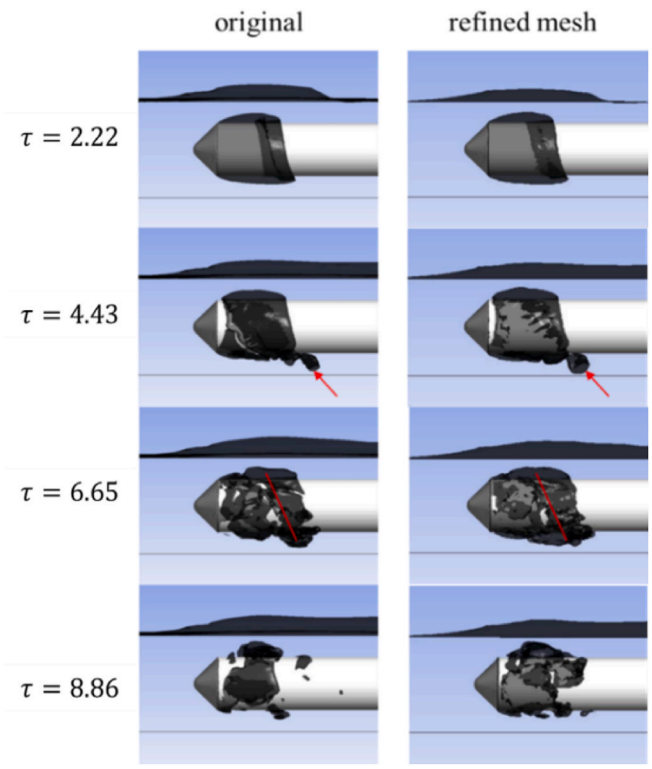

Fig. 25. Comparison between the original mesh and refined mesh simulation results of the cavity evolution at $\tau = 2.22$, $\tau = 4.43$, $\tau = 6.65$, and $\tau = 8.86$ when $d_f/D = d_w/D = 0.405$. Red arrows and lines mark specific characteristics of the cavity. (For interpretation of the references to colour in this figure legend, the reader is referred to the Web version of this article.)

Fig. 22 shows the typical asymmetry cavity profile and partial shedding cavity over the projectile launched near wall. The wall near the cavitating flow can induce partial shedding at the cavity tail. The detailed discussion on the phenomenon can refer to our previous work (Yu et al., 2017; Xu et al., 2018). Here, the partial cavity shedding occurs at the near-wall side of the projectile when d_w/D is less than 0.405.

Fig. 23 shows the typical phenomenon of the natural ventilated cavitating flow that surrounds the projectile. When the projectile is placed very closed to the fee surface, strong entrainment of non-condensable air occurs. The ventilation changes the fluid property inside the cavity, which makes the upper side cavity almost unchanged after growth stage. The discussion on this phenomenon can refer to our previous study (Wang et al., 2017). Natural ventilation occurs on the upper-side cavity when d_f/D is less than 0.081.

It should be noted that some more complex situations may not be reflected in the above flow regimes. Fig. 20 reveals the regimes where typical phenomenon occurs.

5. Conclusions

The cloud cavitating flow that surrounds an axisymmetric projectile in "shallow water" under the mutual effects of the free surface and the bottom wall is analyzed in this article. Both the water tank experiment and numerical simulations are conducted for analyzing the. First, a case with $d_f/D = d_w/D = 0.405$ is discussed. The experimental data and simulation results agree well, which validates the accuracy of the numerical methods. Similar to the conventional cavity the cavity evolution process under the mutual effects also includes four stages: cavity growth, re-entrant jet, cavity shedding and collapsing. However, when placing the projectile near the free surface/wall, the asymmetry cavity shedding, partial cavity shedding, and other specific phenomena will occur.

We have found that the free surface and bottom wall have significant effects on the cloud cavitating flow. The free surface can largely affect the characteristics of the cavity around the projectile. The results show that l and T will decrease with d_f. Inside the cavity, the re-entrant jet is affected by free surface, which can be considered as a "weak" constraint. λ will be tinner as the projectile moving closer to the free surface, thus induce a more stable cavity. Under the near-wall effect, partial cavity shedding occurs on the near-wall side of the projectile. Longer l and T are shown for the cases near wall. For the flow flowing between the lower side of the projectile and the bottom wall, both the dynamic pressure and the momentum become larger compared to the case without bottom wall. The λ becomes thicker as d_w decreases, which makes the cavity less stable. The results also show that the interaction between the upper and lower cavitating flow under the 3D effect will weaken the free surface/near-wall effect.

The vortex structure of the cavitating flow can be visualized based on Q-criterion, which reveals a strong correlation between the cavity evolution and the vortex structure. Different flow regimes are identified in the parameter space spanned by d_f/D and d_w/D. The flow regimes include the entire shedding cavity (symmetry/asymmetry), steady and non-shedding cavity, partial cavity shedding, and ventilated cavity.

In this paper, we analyzed the asymmetric effect of the cavitating flow induced by nearby boundaries. The significant effects of the free surface and wall need to be considered in engineering applications. The cloud cavitating flow over a projectile is complex, which is highly related to the shape of the underwater vehicle. It should be noted that this study is limited to typical working conditions for a typically shaped model, thereby requiring further in-depth analysis.

CRediT authorship contribution statement

Chang Xu: Investigation, Methodology, Formal analysis, Validation, Resources, Writing – original draft, Writing – review & editing. **Jian Huang:** Validation. **Chao Yu:** Data curation. **Yiwei Wang:** Project administration, Writing – review & editing, Supervision, Conceptualization. **Chenguang Huang:** Funding acquisition. **Boo Cheong Khoo:** Supervision.

Declaration of competing interest

The authors declare that they have no known competing financial interests or personal relationships that could have appeared to influence the work reported in this paper.

Acknowledgment

This work was supported by the National Natural Science Foundation of China, grant numbers 11772340, and 11672315, the Youth Innovation Promotion Association CAS (2015015).

Appendix. Verification of Mesh Plan

In order to verify the suitability of the original mesh size for the simulation, we generated a new refined mesh on which the grid near the free surface and the projectile are refined using the same Cartesian cut-cell mesh method. The refined mesh contains about 26.73 million cells. The cavity lengths computed on the two sets of meshes and measured in the experiment are compared in Fig. 24. The results show that the new mesh plan results

agree well with those of the previous model.

The comparison of the cavity profile between the original mesh and refined mesh is shown in Fig. 25 at $\tau = 2.22$, $\tau = 4.43$, $\tau = 6.65$, and $\tau = 8.86$. Features considered for comparison include cavity length, re-entrant jet, partial cavity shedding, and asymmetry cavity shedding, indicated by red arrows and red lines. Although the results show that the mesh does not strictly converge, these two meshes have little effect on the results within this mesh resolution region, which justifies the usability of the original mesh plan.

References

Amromin, E., 2007. Analysis of body supercavitation in shallow water. Ocean Eng. 34 (11), 1602–1606.

Bal, S., 2007. High-speed submerged and surface piercing cavitating hydrofoils, including tandem case. Ocean Eng. 34 (14), 1935–1946.

Bal, S., 2011. The effect of finite depth on 2D and 3D cavitating hydrofoils. J. Mar. Sci. Technol. 16 (2), 129–142.

Bal, S., Kinnas, S., 2002. A BEM for the prediction of free surface effects on cavitating hydrofoils. Comput. Mech. 28 (3–4), 260–274.

Brennen, C.E., 2013. Cavitation and Bubble Dynamics. Cambridge University Press.

Chen, G., Wang, G., Hu, C., Huang, B., Gao, Y., Zhang, M., 2015. Combined experimental and computational investigation of cavitation evolution and excited pressure fluctuation in a convergent–divergent channel. Int. J. Multiphas. Flow 72, 133–140.

Dawson, T.E., 1959. An experimental investigation of a fully cavitating two-dimensional flat plate hydrofoil near a free surface. California Institute of Technology 11 (12), 1651–1655.

Dittakavi, N., Chunekar, A., Frankel, S., Dec 2010. Large eddy simulation of turbulent-cavitation interactions in a venturi nozzle. Journal of Fluids Engineering-Transactions of the Asme 132 (12). Art. no. 121301.

Dular, M., Bachert, R., Stoffel, B., Sirok, B., 2004. Relationship between cavitation structures and cavitation damage. Wear 257 (11), 1176–1184.

Dular, M., Bachert, R., Stoffel, B., Sirok, B., 2005. Experimental evaluation of numerical simulation of cavitating flow around hydrofoil. Eur. J. Mech. B Fluid 24 (4), 522–538.

Faltinsen, O., 2004. Hydrodynamics of high speed marine vehicles. In: Hydrodynamics VI: Theory and Applications: Proceedings of the 6th International Conference on Hydrodynamics. CRC Press, Perth, Western Australia, p. 3, 24-26 November 2004.

Faltinsen, O.M., Semenov, Y.A., 2008. The effect of gravity and cavitation on a hydrofoil near the free surface. J. Fluid Mech. 597, 371–394.

Franc, J.P., Michel, J.M., 2004. Fundamentals of Cavitation. Springer.

Gnanaskandan, A., Mahesh, K., 2015. Large Eddy Simulation of turbulent cavitating flows. In: Presented at the Journal of Physics: Conference Series, Proceedings of the 9th International Symposium on Cavitation. Switzerland.

Gnanaskandan, A., Mahesh, K., 2016. Large Eddy Simulation of the transition from sheet to cloud cavitation over a wedge. Int. J. Multiphas. Flow 83, 86–102.

He, M., Yuan, L., Zhou, L., Yang, J., Wang, Z., 2014. Numerical evaluation of the side wall effect on the flow around a hydrofoil. Eng. Comput. 31 (3), 501–509.

Heindel, T.J., 2011. A review of X-ray flow visualization with applications to multiphase flows. J. Fluid Eng. 133 (7).

Huang, B., Zhao, Y., Wang, G., Mar 20 2014. Large Eddy Simulation of turbulent vortex-cavitation interactions in transient sheet/cloud cavitating flows. Comput. Fluids 92, 113–124.

Hunt, J., 1987. Vorticity and vortex dynamics in complex turbulent flows. Canadian Society for Mechanical Engineering, Transactions 11 (1), 21–35 (ISSN 0315-8977).

Ishida, H., Nuntadusit, C., Kimoto, H., Nakagawa, T., Yamamoto, T., 2001. Cavitation bubble behavior near solid boundaries. http://resolver.caltech.edu/cav2001: sessionA5.003.

Ji, B., Luo, X.-w., Peng, X.-x., Wu, Y.-l., 2013. Three-dimensional large eddy simulation and vorticity analysis of unsteady cavitating flow around a twisted hydrofoil. J. Hydrodyn. 25 (4), 510–519.

Karim, M.M., Prasad, B., Rahman, N., 2014. Numerical simulation of free surface water wave for the flow around NACA 0015 hydrofoil using the volume of fluid (VOF) method. Ocean Eng. 78, 89–94.

Kida, T., Miyai, Y., 1972. Wall effect in cavitating flow past a thin jet-flapped foil. Q. J. Mech. Appl. Math. 25 (1), 83–103.

Kida, T., Miyai, Y., 1975. Lift coefficients on a supercavitating jet-flapped foil between rigid walls. Bulletin of JSME 18 (116), 151–158.

Kimoto, H., Momose, K., Ueki, H., Onishi, T., 1985. A study of a cavitation bubble on a solid boundary. Bulletin of JSME 28 (238), 601–609.

Kunz, R.F., Boger, D.A., Chyczewski, T.S., Stinebring, D., Gibeling, H., Govindan, T., 1999. Multi-phase CFD analysis of natural and ventilated cavitation about submerged bodies. Proceedings of FEDSM 99, 1–9.

Kunz, R.F., et al., Nov 2000. A preconditioned Navier-Stokes method for two-phase flows with application to cavitation prediction. Comput. Fluids 29 (8), 849–875.

Leroux, J.B., Coutier-Delgosha, O., Astolfi, J.A., 2005. A joint experimental and numerical study of mechanisms associated to instability of partial cavitation on two-dimensional hydrofoil. Phys. Fluids 17 (5), 052101.

Li, L., Jia, Q., Liu, Z., Li, B., Hu, Z., Lin, Y., 2015. Eulerian two-phase modeling of cavitation for high-speed UUV using different turbulence models. In: Cyber Technology in Automation, Control, and Intelligent Systems (CYBER), 2015 IEEE International Conference on. IEEE, pp. 1247–1252.

Liang, H., Sun, L., Zong, Z., Zhou, L., Zou, L., 2013. Analytical modelling for a three-dimensional hydrofoil with winglets operating beneath a free surface. Appl. Math. Model. 37 (5), 2679–2701.

Muzaferija, S., 1999. A two-fluid Navier-Stokes solver to simulate water entry. In: Proceedings of 22nd Symposium on Naval Architecture, vol. 1999. National Academy Press, pp. 638–651.

Owis, F.M., Nayfeh, A.H., 2004. Numerical simulation of 3-D incompressible, multi-phase flows over cavitating projectiles. Eur. J. Mech. B Fluid 23 (2), 339–351.

Robert, J.W.D., Knapp, T., Hammitt, G., 1970. Cavitation. McGraw-Hill.

Roohi, E., Zahiri, A.P., Passandideh-Fard, M., May 1 2013. Numerical simulation of cavitation around a two-dimensional hydrofoil using VOF method and LES turbulence model. Appl. Math. Model. 37 (9), 6469–6488.

Sahner, J., Weinkauf, T., Hege, H.-C., 2005. Galilean invariant extraction and iconic representation of vortex core lines. EuroVis 151–160.

Wang, G., Ostoja-Starzewski, M., Mar 2007. Large eddy simulation of a sheet/cloud cavitation on a NACA0015 hydrofoil. Appl. Math. Model. 31 (3), 417–447.

Wang, G., Senocak, I., Shyy, W., Ikohagi, T., Cao, S., 2001. Dynamics of attached turbulent cavitating flows. Prog. Aero. Sci. 37 (6), 551–581.

Wang, Y., Wu, X., Huang, C., Wu, X., 2016a. Unsteady characteristics of cloud cavitating flow near the free surface around an axisymmetric projectile. Int. J. Multiphas. Flow 85, 48–56.

Wang, Y., Wu, X., Huang, C., 2016b. Ventilated partial cavitating flow around a blunt body near the free surface. In: ISROMAC 2016: International Symposium on Transport Phenomena and Dynamics of Rotating Machinery, p. 6.

Wang, Y., Huang, C., Fang, X., Yu, X., Wu, X., Du, T., 2016c. Cloud cavitating flow over a submerged axisymmetric projectile and comparison between two-dimensional RANS and three-dimensional large-eddy simulation methods. J. Fluid Eng. 138 (6).

Wang, Y., Xu, C., Wu, X., Huang, C., Wu, X., 2017. Ventilated cloud cavitating flow around a blunt body close to the free surface. Physical Review Fluids 2 (8), 084303.

Whitham, G.B., 2011. Linear and Nonlinear Waves. John Wiley & Sons.

Wu, X.C., Wang, Y.W., Huang, C.G., 2015. Effect of mesh resolution on large eddy simulation of cloud cavitating flow around a three dimensional twisted hydrofoil. Eur. J. Mech. B Fluid 55 (1), 229–240.

Xie, N., Vassalos, D., 2007. Performance analysis of 3D hydrofoil under free surface. Ocean Eng. 34 (8), 1257–1264.

Xin, C., Lu, C.-j., Jie, L., Pan, Z.-c., 2008. The wall effect on ventilated cavitating flows in closed cavitation tunnels. Journal of Hydrodynamics, Ser. B 20 (5), 561–566.

Xin, C., Lu, C.-j., Jie, L., Ying, C., 2011. Properties of natural cavitation flows around a 2-D wedge in shallow water. Journal of Hydrodynamics, Ser. B 23 (6), 730–736.

Xu, C., Wang, Y., Huang, C., Yu, C., Huang, J., 2017. Cloud cavitating flow that surrounds a vertical hydrofoil near the free surface. J. Fluid Eng. 139 (10), 101302.

Xu, C., Wang, Y., Huang, C., Yu, C., Huang, J., 2018. Analysis of Near-wall effect on cloud cavitating flow that surrounds an axisymmetric projectile using large eddy simulation with Cartesian cut-cell mesh method. Eur. J. Mech. B Fluid 67, 15–24.

Yan-Peng, W., Yi-Wei, W., Xin, F., Chen-Guang, H., Zhu-Ping, D., 2011. A scaled underwater launch system accomplished by stress wave propagation technique. Chin. Phys. Lett. 28 (2), 024601.

Yu, C., Wang, Y., Huang, C., Du, T., Xu, C., Huang, J., 2017. Experimental and numerical investigation on cloud cavitating flow around an axisymmetric projectile near the wall with emphasis on the analysis of local cavity shedding. Ocean Eng. 140, 377–387.

Yu, X., et al., May 2014. Study of characteristics of cloud cavity around axisymmetric projectile by large eddy simulation. Journal of Fluids Engineering-Transactions of the Asme 136 (5), 051303. Art. no.

Zhou, J.-J., Yu, K.-P., Min, J.-X., Ming, Y., 2010. The comparative study of ventilated super cavity shape in water tunnel and infinite flow field. Journal of Hydrodynamics, Ser. B 22 (5), 689–696.

Zwart, Philip, Gerber, A.G., Belarmri T., A Two-phase on Model for Predicting Cavitation Dynamics ([Online]).